Materials Horizons

ROYAL SOCIETY OF CHEMISTRY

COMMUNICATION

View Article Online
View Journal

Cite this: DOI: 10.1039/d5mh02110c

Received 5th November 2025,
Accepted 1st April 2026

DOI: 10.1039/d5mh02110c

rsc.li/materials-horizons

All-solution-processed mid-infrared electrochromics (ASPIRE) for thermoregulation with arbitrary curvatures

Pei-Jan Hung,[a] Qizhang Li,[a] Ting-Hsuan Chen,[ab] Xubing Wu,[a] Ching-Tai Fu,[a] Yu Han,[a] Ronghui Wu,[a] Gangbin Yan,[a] Qingsong Fan,[a] Yunhao Zhao,[a] Jiadong Liu,[a] Pin-Ruei Huang,[a] Yuanke Chen,[a] Chenxi Sui,[a] Genesis Higueros,[ab] Alex Flores,[a] Fengyuan Shi[c] and Po-Chun Hsu *[a]

Mid-infrared electrochromism provides a powerful approach to dynamically regulate radiative heat transfer, with important implications for building energy efficiency, industrial process optimization, spacecraft thermal control, and personal heat management. However, most reported mid-IR electrochromic devices are fabricated on planar substrates, limiting their adaptability to three-dimensional (3D) or curved surfaces. When applied to such geometries, these devices fail to conform fully, introducing air gaps that increase thermal contact resistance and reduce radiative modulation efficiency. Here, we report an all-solution-processed fabrication methodology that enables electrochromic devices to be directly formed on arbitrarily curved 3D surfaces, effectively transforming the object into an electrically tunable thermal emitter. The device employs poly(3,4-ethylenedioxythiophene):polystyrene sulfonate (PEDOT:PSS) as both the electrochromic and charge-storage layers, separated by a heterogeneous mixed ionic–electronic conductor composed of HNO_3-doped carbon nanotubes and crosslinked polyacrylamide/lithium chloride hydrogel. This layer-by-layer configuration ensures complete surface conformity and robust electrochemical performance. The resulting mid-IR electrochromic system achieves an emissivity tunability of 0.195 and an apparent temperature modulation of 6.1 °C on planar substrates and 2.3 °C on curved objects. This work establishes a generalizable strategy for outward-facing electrochromic devices, offering broad opportunities for advanced light and heat management technologies.

New concepts

Traditional electrochromic devices adopt a multilayer sandwich architecture with transparent electrodes enclosing the electrochromic and electrolyte layers. While suitable for visible modulation, this design is ineffective in the mid-infrared (mid-IR) region because conventional electrodes strongly absorb IR light, limiting emissivity tunability and overall efficiency. Here, we introduce a new design principle in which the electrochromic layer is positioned as the outermost surface and coupled with a heterogeneous mixed ionic–electronic conductor composed of carbon nanotube (CNT) networks, polyacrylamide hydrogels, and PEDOT:PSS. This architecture minimizes IR absorption by the electrodes while maintaining efficient electronic and ionic transport, enabling large, reversible mid-IR modulation. Moreover, our all-solution-processable fabrication strategy allows seamless integration of the device onto arbitrarily curved three-dimensional surfaces, effectively transforming them into dynamically tunable thermal emitters. This concept establishes a new materials and device design strategy for mid-IR electrochromics, unifying electronic, ionic, and optical functionalities in a single, conformable platform for radiative heat management.

Introduction

Thermal stability is a crucial function for almost all sophisticated devices, whether it is artificial electronics or living animals and humans. Over the past decade, the exacerbating effects of global warming have demanded even more studies in this aspect and have driven a significant amount of research into mid-IR electrochromism as an innovative and efficient approach for dynamic thermoregulation.[1] Recent comprehensive reviews have highlighted the rapid evolution of these materials, ranging from photothermal modulation for efficient solar harvesting to variable-emissivity surfaces for radiative cooling.[2,3] By actively modulating overall thermal emittance, users can personalize radiative heat transfer with minimal energy input, mitigating the impact of environmental temperature fluctuations.[4] Compared with actively supplying thermal energy to maintain temperature, the variable emissivity approach can achieve the same goal with extremely low energy consumption, which has been widely adopted by much research for dynamic thermoregulation.[5–13] In recent years, applications in building thermoregulation,[13–15] radiative cooling,[16] spacecraft thermal control,[17,18] and personal thermal management[4,7,19] have been explored extensively. Among various infrared electrochromic materials, conjugated

[a] Pritzker School of Molecular Engineering, University of Chicago, Chicago, IL 60637, USA. E-mail: pochunhsu@uchicago.edu
[b] Thomas Lord Department of Mechanical Engineering and Materials Science, Duke University, Durham, NC 27708, USA
[c] Electron Microscopy Core, University of Illinois Chicago, Chicago, IL 60607, USA

polymers stand out as particularly promising due to their chemical tunability and solution processability,[20] making them suitable for industrial-scale applications. These unique properties make conjugated polymers indispensable for advancing dynamic thermoregulation applications from laboratory research to industrial-scale implementation.

The solution processability of conjugated polymers provides a unique advantage for translating laboratory demonstrations into scalable devices. These materials can be dispersed or dissolved in a solvent, and deposited by methods such as spray coating,[21–23] roll-to-roll coating,[22] inkjet printing,[22,24] or spin coating.[23] Well-studied conjugated polymers, such as polyaniline (PANI), poly(3-hexylthiophene-2,5-diyl) (P3HT), and PEDOT:PSS, have been fabricated on rigid, flexible, and stretchable substrates[25] demonstrating their versatility. Despite these advances, leveraging solution-processed conjugated polymers for mid-IR electrochromic devices on non-planar or three-dimensional surfaces remains an unresolved challenge (Table S1).

Conjugated polymer-based infrared electrochromics control the radiative heat loss by modulating the carrier density and mid-IR reflectivity (thus the thermal emissivity, according to Kirchhoff's law).[25,26] However, most existing mid-IR electrochromic devices are fabricated on flat, planar surfaces, leaving largely unexplored applications on three-dimensional (3D) and curved objects. While planar substrates have been successfully employed in advanced smart windows – achieving multifunctional control over visible transparency, near-infrared solar heat gain, and even photothermal regulation[15,27–29] – they are fundamentally incompatible with the geometric requirements of personal thermal management on curved bodies. Unlike visible light modulation which operates *via* transmission, effective radiative cooling requires intimate thermal contact between the emitter and the heat source. Using a rigid planar device on a curved surface inevitably creates insulating air gaps, which introduce significant thermal contact resistance and thermally decouple the device from the object, thereby nullifying the thermoregulatory effect. As shown in Fig. 1a, using a premade two-dimensional planar device to conform to a complexly curved object's surface without introducing folding or distortion is impossible. According to Gauss's Theorem Egregium,[30] at any point on a curved surface with principal curvatures κ_1 and κ_2, its Gaussian curvature $K = \kappa_1\kappa_2$ is an intrinsic property that remains unchanged unless the surface is stretched. This theorem explains why a premade planar device ($\kappa_{1,dev} = \kappa_{2,dev} = 0$, $K_{dev} = 0$) cannot conformally wrap a 3D curved object with non-zero curvature ($K_{obj} \neq 0$). Failing to achieve a conformal and close contact between the modulating device and the object inevitably creates a considerable thermal contact resistance (*e.g.*, air gap), significantly reducing thermoregulation performance. To resolve this challenge, we develop a solution-processed electrochromic device that can be directly fabricated onto the 3D curved object surface, allowing it to conform perfectly to the curvature of the base object and eliminate the air gaps. These limitations highlight the need for innovative fabrication processes to conformally render 3D surfaces with tunable electrochromic properties for effective mid-IR thermoregulation.

In this article, we demonstrate an all-solution-processed fabrication process that can render the surface of diverse 3D curved objects with electrochromic dynamic tunability, particularly in the mid-IR regime. With the rational material design of CNT bundles and PEDOT:PSS, a heterogeneous mixed ionic–electronic conductor was realized, allowing the PEDOT:PSS to be the outermost layer while remaining electrochemically active for tunable thermal emission. The solution-processed device shows an emissivity tunability of $\Delta\varepsilon = 0.195$ with minimal decay even after 500 cycles. Heat transport calculations suggest that the electrochromic device can stabilize the temperature against fluctuations of 4.2 °C under mild convection ($h = 3$ W m^2 K^{-1}). Our work offers a robust pathway for scalable, solution-processed devices, paving the way for future advanced thermal regulation and optical applications on complex 3D surfaces.

The design principles

The design principles for mid-IR electrochromic devices differ fundamentally from those of their visible-light counterparts. Conventional visible electrochromic devices typically adopt a symmetric architecture, in which two transparent conducting electrodes sandwich the electrolyte and electrochromic layer. This configuration, however, is not suitable for mid-IR devices because standard transparent conductors such as indium tin oxide (ITO) and aluminum-doped zinc oxide (AZO) exhibit strong absorption in the infrared regime. Moreover, practical mid-IR applications demand flexibility and compatibility with 3D curved geometries, where rigid substrates such as calcium fluoride and barium fluoride are unsuitable. Graphene, while intrinsically transparent in the mid-IR, solution-processable, and electrically conducting, often develops wrinkles and folds during deposition and post-treatment, severely degrading its electrical performance.

To overcome these challenges, we propose the use of carbon nanotubes combined with PEDOT:PSS as the outermost conductive layer for 3D curved surfaces. A critical requirement for this asymmetric design is the use of conjugated polymers with intrinsically high conductivity, since their electrical properties directly govern infrared tunability. If the polymer is insufficiently conductive, oxidation fails to generate a sufficiently high carrier density to push the plasma frequency above the mid-IR range. Instead of becoming reflective, the polymer behaves as a lossy dielectric that strongly absorbs incident radiation, resulting in a persistently high emissivity and poor modulation depth. By contrast, highly conducting systems such as PEDOT:PSS and our in-house synthesized PANI ($\sigma > 200$ S cm^{-1}, see Note S2) enable effective electrochemical doping and dedoping, producing pronounced changes in mid-IR emissivity (Fig. S1). PEDOT:PSS is particularly suitable because its mid-IR properties are electrochemically tunable: oxidation generates mobile charge carriers (polarons and bipolarons)[31] (Fig. 1b) that increase infrared reflectivity, while reduction (dedoping) removes carriers from the PEDOT backbone, thereby enhancing infrared emissivity. While the optical modulation arises from carrier density changes in PEDOT:PSS, the choice of ionic conductor strongly influences how efficiently these changes occur (see Note S3).

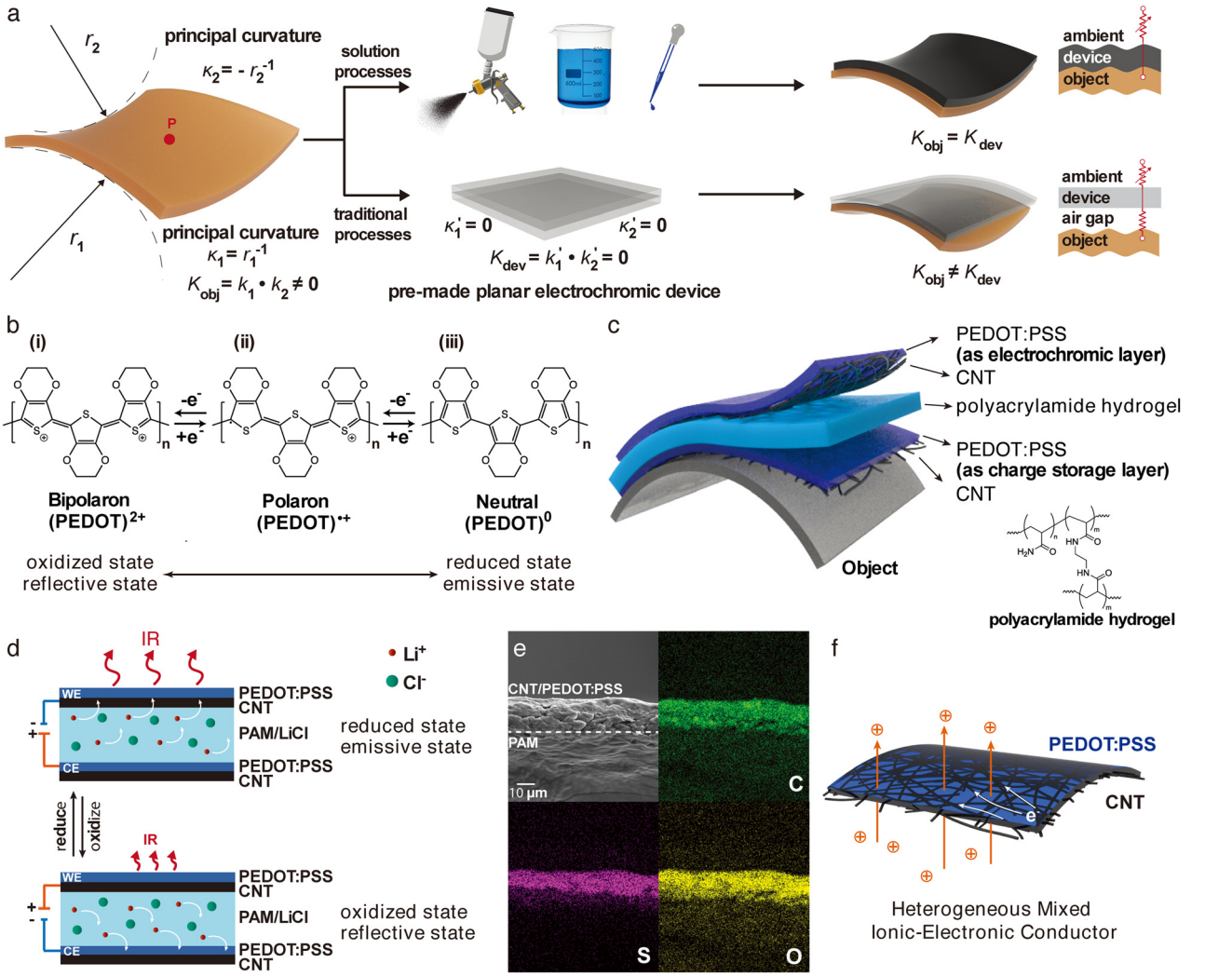

Fig. 1 Design principles of the all-solution-processed mid-IR electrochromic (ASPIRE) device. (a) The advantages of solution processability: traditional 2D planar electrochromic devices cannot fully conform to 3D curved objects, leading to air gaps that act as thermal resistance and reduce the efficacy of thermoregulation. The proposed all-solution-processed fabrication methodology enables the creation of conformal electrochromic devices on arbitrarily curved 3D surfaces. (b) Schematic of PEDOT:PSS in its oxidation and reduction states. (i) Bipolaron chain (oxidized state, reflective), (ii) polaron chain, and (iii) neutral chain (reduced state, emissive). The plasma frequency varies with the charge carrier density, enabling dynamic emissivity modulation. (c) The structure of the ASPIRE device is designed as an asymmetric layered electrochemical cell configuration. The top PEDOT:PSS layer acts as a tunable thermal emitter, ensuring that modulated thermal radiation is emitted. The bottom PEDOT:PSS layer acts as a charge reservoir. The inset shows the chemical structure of polyacrylamide (PAM) hydrogel as the electrolyte. (d) Mechanism of ion movement between the PAM/LiCl hydrogel electrolyte and CNT networks during electrochemical oxidation and reduction. (e) Scanning electron microscope (SEM) and energy dispersive X-ray spectroscopy (EDX) mappings of the ASPIRE device cross-section. The images show that PEDOT:PSS penetrates the CNT network layer, establishing contact with the PAM hydrogel electrolyte. (f) Schematics of the heterogeneous mixed ionic–electronic conductor. The CNT network maintains PEDOT:PSS on curved surfaces while providing horizontal electrical conductivity. PEDOT:PSS enables vertical ion transport and drives electrochromic reactions.

In this work, the ASPIRE device strategy is to regulate radiative heat flux through mid-IR emissivity modulation (Kirchhoff's law), rather than through changes in thermal conductivity. Further details are provided in Notes S1–S3 and Fig. S2.

To capitalize on these tunable mid-IR properties, the ASPIRE device employs a carefully engineered asymmetric layered architecture (Fig. 1c), distinct from the traditional "sandwich" structure of visible-light devices. In this configuration, while both the working and counter electrodes utilize CNT networks as current collectors, the configuration of the active material is asymmetric: the top PEDOT:PSS layer infiltrates the CNT electrode and serves as the outermost active thermal emitter to maximize radiative exchange, while the bottom PEDOT:PSS layer functions as the buried charge-storage layer. This outward-facing design eliminates the need for a top infrared-blocking electrode/substrate, which is a limiting factor in conventional symmetric electrochromic cells.

Building on this asymmetric architecture, the device incorporates additional functional layers to enhance charge and ion transport (Fig. 1d–f). Beneath the outer PEDOT:PSS layer, a single-walled CNT network on a PAM/LiCl hydrogel forms a heterogeneous mixed ionic–electronic conductor. The CNTs provide porous electrical pathways for lateral electron transport,

while simultaneously offering channels for vertical ion migration. Their hydrophilic nature also helps retain PEDOT:PSS, ensuring adhesion to curved surfaces and intimate contact with the PAM/LiCl hydrogel. SEM and EDX analyses (Fig. 1e) confirm that sulfur from PEDOT:PSS penetrates through the CNT network into the underlying PAM. As an organic mixed ionic–electronic conductor (OMIEC), PEDOT:PSS further expands redox-active sites, enhances current density, and functions as the electrochromic layer. Together, these components establish efficient redox reactions at the triple-phase boundary of PEDOT:PSS, CNTs, and PAM, even on complex 3D curved geometries.

While the in-house synthesized PANI exhibits a larger emissivity modulation due to its superior conductivity (Fig. S1), we strategically selected PEDOT:PSS as the primary active material for the ASPIRE device. This choice is driven by the critical requirements for environmental safety and scalable green processing. Unlike high-performance PANI, which typically relies on toxic and corrosive organic solvents (*e.g.*, *m*-cresol) to induce secondary doping, PEDOT:PSS is processed from an aqueous dispersion. This eliminates the need for hazardous solvents, ensures compatibility with diverse substrates, and provides a commercially reproducible standard for all-solution-processed thermal management devices.

The heterogeneous mixed ionic–electronic conductor

The advantages of CNTs for a successful ASPIRE are threefold: (i) acid-treated CNTs retain high-COOH functional groups, facilitating good dispersion in a polar solvent for solution processability.[32] The high hydrophilicity of these CNT networks also allows the PEDOT:PSS aqueous solution to penetrate the CNT networks and to contact the PAM/LiCl hydrogel electrolyte to facilitate vertical ion transportation. (ii) CNTs are stable at the operating redox potential of PEDOT:PSS around ±1.1 V *versus* Ag/AgCl.[33] Silver nanowires (AgNWs) are also widely used as a solution-processed current collector. However, their low oxidizing potential (0.8 V *vs.* SHE) makes them prone to oxidation and corrosion, thereby compromising the cycle life stability of the device (Fig. S3). (iii) CNTs tend to aggregate and form bundles during solvent evaporation due to the van der Waals forces. These bundles consist of up to ten to hundreds of single-walled carbon nanotubes, each several microns long, arranged in a hexagonal close-packed structure.[34–37] When the CNT-dispersed solution is sprayed onto a substrate, the densely packed bundles interconnect, forming random CNT networks. The random networks establish a horizontal electrical pathway while the pores provide vertical channels for ion movement (Fig. 2a–d).

The morphology of the CNT networks was characterized by electron microscopy. Due to the van der Waals forces, individual CNTs represent only a tiny portion (less than 5%) of the dispersion solution, as shown in the low-angle annular dark field scanning transmission electron microscopy (LAADF-STEM) image in Fig. 2b. The individual CNT has a diameter of approximately 1.8 nm. In Fig. 2c, the high-resolution transmission electron microscope (HR-TEM) image shows a CNT bundle with a diameter of 11 nm. When the CNT-dispersed solution was sprayed onto a substrate, numerous CNT bundles aggregated to form porous CNT networks, as shown in the scanning electron microscope (SEM) image in Fig. 2d. Fig. 2e illustrates the size distribution of the CNT bundles, exhibiting a predominantly Gaussian distribution, with over 50% of the bundle diameters falling within the 10–15 nm range. The pore size distribution of CNTs was further quantified using the non-local density functional theory (NLDFT) model, based on the measured N_2 adsorption isotherm. As shown in Fig. S4, the CNTs have mesopores (mainly 10–50 nanometers) and micropores (1–2 nanometers), consistent with the electron microscopy results. The consistency of the CNT bundle and pore size distribution provides a network structure for efficient horizontal electrical transport through the CNT bundles and vertical ionic transport through the pores. Raman spectroscopy (Fig. 2f) also confirms the CNT molecular structure and its pristine, low-defect quality.

To fabricate a stable and reversible electrochromic device, it is crucial to lower the DC electrical resistance and provide a uniform electric field for the electrochemical redox reactions. The electrical sheet resistance R_s is controlled by the amount of CNT networks, governed by the equation below:

$$R_s = \frac{\rho}{t} \sim \frac{1}{t} \propto \frac{1}{m} \quad (1)$$

where ρ is the bulk electrical resistivity, t is the thickness of the CNT layer, and m is the CNT mass loading per unit area. This inverse relationship between the sheet resistance of the substrate and the areal mass loading of CNTs is clearly shown in Fig. 2g. With the increased amount of the CNT spray-coated onto the glass substrate, the sheet resistance of the glass slides is significantly reduced to about 9 Ω sq^{-1}. However, as the amount of CNT increases, the vertical diffusion length and tortuosity for ions also increase. Recent studies on porous carbon electrodes have shown that high tortuosity restricts long-range ionic diffusion, thereby increasing ionic resistance.[38,39] This indicates that there is an optimal areal mass loading that provides both low electrical resistance and high ionic conductance, which will be discussed later.

To optimize the thickness of the CNT on PAM/LiCl hydrogel as a heterogeneous mixed ionic–electronic conductor, the ionic conductance was measured as a function of thickness. Firstly, the ionic conductivity of a pristine PAM/LiCl hydrogel electrolyte was measured by electrochemical impedance spectroscopy (EIS). Fig. 2h shows the Nyquist plot of the pristine PAM/LiCl hydrogel electrolyte, measured with two stainless-steel blocking electrodes. The result exhibits typical non-ideal capacitive behavior, typically modeled by a constant phase element (CPE) connected in series to a resistor (R_s) due to the electrolyte's high ionic conductivity and the absence of Faradaic reactions. The ionic conductivity of the PAM/LiCl hydrogel calculated from the *x*-axis intercept is 63.6 ± 15 mS cm^{-1}, which is higher than that of most reported gel polymer electrolytes.[40–42] Additionally, as shown in Fig. S5, in the PAM/PEDOT:PSS configuration, the hydrogel effectively sustains ion transport to the PEDOT:PSS layer, thereby maintaining high ionic conductivity. Inductively coupled plasma mass spectrometry (ICP-MS) further confirms that polyacrylamide hydrogel contains an extremely high LiCl

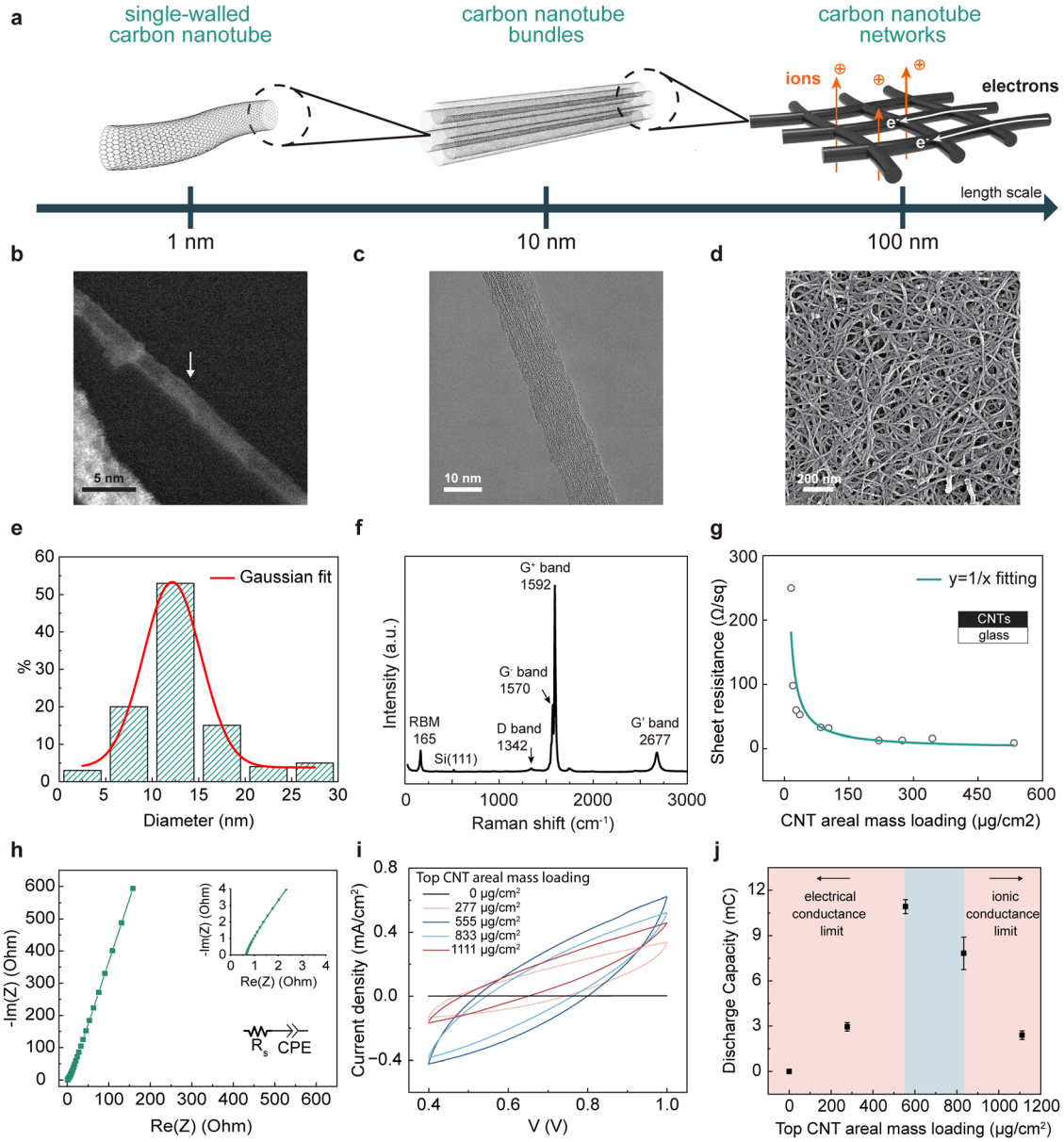

Fig. 2 Carbon nanotube networks as a heterogeneous mixed ionic–electronic conductor. (a) Length scale of CNTs as single tubes, bundles, and networks (not drawn to scale). The pores within the CNT networks facilitate vertical ionic transport through PEDOT:PSS, while the CNT networks enable horizontal electronic transport. (b) Low-angle annular dark-field scanning transmission electron microscopy (LAADF-STEM) image of a single CNT. (c) High-resolution transmission microscope (HR-TEM) image of a CNT bundle. (d) SEM image of CNT networks. (e) Diameter distribution of CNT bundles observed in (d), showing that most CNT bundles have diameters in the range of 12–16 nanometers. (f) Raman spectrum of CNTs, confirming their molecular structure and quality. (g) Relationship between sheet resistance and CNT areal mass loading on a glass substrate. The sheet resistance decreases proportionally with the inverse of CNT mass loading, demonstrating improved electrical conductivity with increased CNT deposition. (h) Nyquist plot of a pristine PAM/LiCl hydrogel electrolyte measured with two stainless-steel blocking electrodes, showing high ionic conductivity without charge transfer reactions. (i) Cyclic voltammetry curves of planar ASPIRE devices with varying top-layer CNT mass loadings (0–1111 μg cm^{-2}). The control sample (0 μg cm^{-2}) exhibits negligible current response, confirming the necessity of the CNT network for overcoming the IR drop. Scan rate: 100 mV s^{-1}. (j) Discharge capacity (Q_{dis}) *versus* top-layer CNT areal mass loading on PAM/LiCl hydrogel electrolyte, calculated by integrating the cathodic currents from (i). The shaded regions illustrate the trade-off mechanism: the device transitions from an electrical conductance-limited regime (low loading, pink) to an ionic conductance-limited regime (high loading, pink). The central blue band highlights a broad optimal window (555–833 μg cm^{-2}) where electronic and ionic transport are balanced, with the 555 μg cm^{-2} condition yielding the maximum accessible capacity.

concentration (10.72 M), which directly accounts for its excellent ionic conductivity. This high salt content also represents an effective strategy to expand the electrochemical stability window (Note S4), meeting the device's operational requirements.

Finally, to optimize the heterogeneous mixed ionic–electronic conductor, we investigated the electrochemical performance as a function of the top-layer CNT areal mass loading. In this experimental series, the bottom-layer CNT electrode and

the quantity of PEDOT:PSS were kept constant to strictly isolate the influence of the top CNT network. The quantity of the top-layer CNT sprayed is normalized from standardized spray amounts (2.5, 5.0, 7.5, and 10.0 mg of CNTs) over a 3 × 3 cm^2 active area to yield areal densities of 277, 555, 833 and 1111 μg cm^{-2}, respectively.

Fig. 2i presents the cyclic voltammetry (CV) evolution. The control sample (0 μg cm^{-2} CNT) exhibits negligible current, confirming that without the CNT scaffold, the dense PEDOT:PSS layer suffers from high IR drop and limited ion accessibility. Upon introducing CNTs, the redox current increases significantly. However, simply adding more CNTs does not monotonically improve performance.

To quantify this, we calculated the discharge capacity (Q_{dis}) by integrating the cathodic current from the CV scans (Fig. 2i) The results in Fig. 2j reveal a distinct trade-off mechanism governing the device performance. At low loadings (< 555 μg cm^{-2}), the device is electronically limited, lacking sufficient percolation pathways for efficient charge collection. Conversely, at high loadings (> 833 μg cm^{-2}), as the increased thickness and tortuosity of the CNT network restrict vertical ion diffusion. Notably, the data identifies a broad optimal window (highlighted in blue) where the device performance is maximized. Within this regime, the 555 μg cm^{-2} loading yield the highest redox capacity and was therefore selected as the representative condition for subsequent 3D device fabrication.

Mid-IR electrochromic property characterization and simulation

The ASPIRE devices were first fabricated on planar substrates to validate the solution-processability and mid-IR electrochromic performance. As shown in Fig. 3a, the planar ASPIRE device can be tuned between a low-emissivity (oxidized/doped) state and a high-emissivity (reduced/dedoped) state, using chronoamperometry (CA) in a two-electrode configuration. The FTIR results confirm that the structural design effectively facilitates ion transport from the hydrogel electrolyte to the outermost layer of PEDOT:PSS, enabling electrochromic performance. Moreover, by adopting the ''water-in-salt'' hydrogel strategy, the electrochemical operating potential is successfully expanded to 4.67 V (Note S4 and Fig. S7). For subsequent experiments, an operational potential window of ±2 V was chosen to maximize the IR tuning performance. A constant potential of 2 V (for the low-ε/doped state) and −2 V (for the high-ε/dedoped state) was applied for 3 minutes each, totaling 6 minutes per cycle to ensure complete reduction or oxidation of the top layer of PEDOT:PSS. The CA data in Fig. S8 and S9 show that the ASPIRE device performs stable and consistent electrochemical reactions during oxidation and reduction cycles. This yields an IR emissivity tunability (Δε) of 0.195, which is defined as the difference between the high- and low-emissivity states, using weight-averaged emissivity calculated based on blackbody radiation at a typical human skin temperature (34 °C). The corresponding emissivity modulation is directly visualized by IR thermal images, as shown in Fig. 3b and S10, where the device was placed on a 50 °C hotplate as the background. The apparent temperature of the device has a 6.1 °C temperature difference (39.2 °C–33.1 °C) solely because of the emissivity changes, demonstrating its excellent capability for thermoregulation applications. Meanwhile, no visible color change is observed (Fig. S11), as the broadband absorption of the CNT network dominates the optical appearance and effectively masks any subtle color variations from PEDOT:PSS.

To further verify long-term stability, we next examined the *in situ* emissivity tuning kinetics and cycle life of the ASPIRE device. Fig. 3c shows the ASPIRE device's *in situ* emissivity tuning kinetics and cycle life measurement. Each data point represents the weight-averaged emissivity (ε_{avg}) measured by Fourier-transform infrared spectroscopy (FTIR) based on Kirchhoff's law. The high-emissivity state (−2 V, blue) and the low-emissivity state (2 V, red) represent the measurements of the ASPIRE device in its reduced and oxidized states, respectively, after three minutes of electrochemical reduction/oxidation. The Δε (turquoise) is the emissivity difference between the two states. The results reveal that the planar ASPIRE device can reversibly switch between the high- and the low-emissivity states and sustain nearly 500 cycles with only a 27% decrease in Δε.

Notably, Δε increases slightly by 4% after 118 cycles, likely due to the activation of the ASPIRE device. The device exhibited a gradual increase in emissivity modulation depth during the initial cycles, stabilizing around the 118th cycle. This phenomenon is attributed to the electrochemical activation of the polymer network.[43] The high-concentration water-in-salt electrolyte possesses a significantly higher viscosity due to dense ion–ion interactions, slowing its infiltration into the nanoporous composite. Concurrently, repeated cycling provides the conformational activation energy to relax the initially compact polymer chains. Thus, stabilization signifies the thermodynamic equilibrium where the viscous electrolyte has fully permeated and the polymer network is structurally relaxed.

The insets (Fig. 3c(i) and (ii)) show *in situ* FTIR weight-averaged emissivity evolution data recorded by a Thermo Fisher Nicolet™ iS50 FTIR time-series program, with 8 second intervals. Fig. 3c(i) highlights the dynamic emissivity evolution between the 118th and 123rd cycles, where the oxidation process proceeds more rapidly than the reduction process. This asymmetry is further quantified by analysis of the switching kinetics (Fig. S12), yielding characteristic times of $\Delta t_{red} \approx 161$ s and $\Delta t_{oxi} \approx 57$ s, consistent with previous reports that dedoping in PEDOT:PSS is slower due to higher activation barriers.[44–46] Fig. 3c(ii) displays similar emissivity evolution data from the 439th to 444th cycle, demonstrating consistent switching behavior even after extended cycling. With the cycling performance and stability established, we next explore how the emissivity modulation translates to practical thermoregulation capability.

To explore the thermoregulation capability of the ASPIRE device, we theoretically analyze its ability to control the radiative heat exchange using the experimentally measured emissivity (Fig. 3a), as shown in Fig. 3e and f and Fig. S13–S15 (see Note S5 for details). In Fig. S13, changing the ASPIRE device's

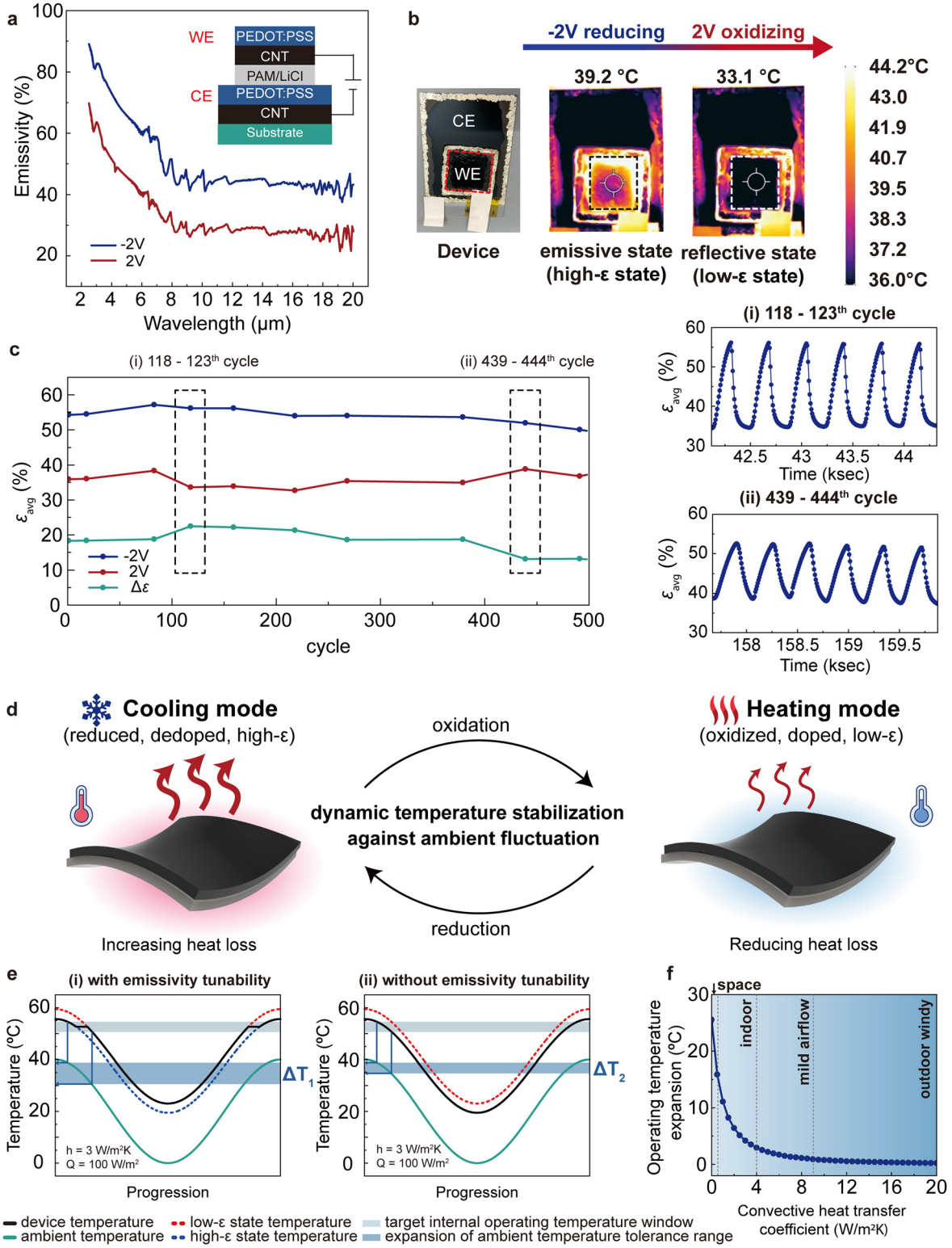

Fig. 3 Dynamic mid-IR electrochromic properties characterization and thermoregulation simulations. (a) Emissivity spectra of the planar ASPIRE device on a glass substrate at high (−2 V) and low emissivity state (2 V) emissivity states at room temperature. The inset illustrates the device structure schematics. WE: working electrode. CE: counter electrode. (b) Photo of the planar ASPIRE device and corresponding IR thermal images in both high- and low-emissivity states. Full electrochemical reaction images can be found in Fig. S10 and Movie S1. (c) Time series of cyclic emissivity spectra, where each data point represents the weight-averaged emissivity (ε_{avg}) based on blackbody radiation at human body temperature (34 °C). The insets show time-series emissivity evolution during specific cycles: (i) 118th–123rd cycle, and (ii) 439th–444th cycle (6 min per cycle), with each data point sampled at eight-second intervals. (d) Schematic illustration of the ASPIRE device dynamically stabilizing temperature against ambient fluctuations. (e) Simulation of operating temperature expansion under an indoor mild convection environment (h = 3 W m^2 K^{-1}), comparing ASPIRE devices (i) with and (ii) without

emissivity tunability. Turquoise line: ambient temperature; black line: ASPIRE device temperature; red dashed line: device temperature fixed in the low-ε state; blue dashed line: device temperature fixed in the high-ε state; the light blue band marks the device's internal operating window ($T_{dev}^{max} - 1$ °C to $T_{dev}^{max} - 5$ °C). The dark blue span represents the ambient temperature range over which the device remains within this operating window. ΔT_1 corresponds to this range with emissivity tunability, while ΔT_2 corresponds to the case without tunability. The operating temperature expansion is defined as $\Delta T_1 - \Delta T_2$. (f) Calculated operational temperature range expansion under various convection coefficients. See Note S6 for details.

emissivity can effectively control the radiative heat flux. For instance, at a fixed device temperature of 30 °C and an ambient temperature of 0 °C, the ASPIRE device can tune the radiative heat flux from 42.0 W m^{-2} at the low-ε state to 68.8 W m^{-2} at the high-ε state.

As shown in Fig. 3d, with its dynamic thermoregulation capability, ASPIRE can stabilize an object's temperature against ambient fluctuations, effectively expanding the usable operating range for electronic devices. In the context of living animals – particularly humans – this corresponds to the "thermal comfort zone". As an illustrative case, we consider a constant heat generation of $Q = 100$ W m^{-2} with sinusoidal ambient fluctuation between 0 °C and 40 °C under mild conduction/convection (h = 3 W m^2 K^{-1}) (Fig. 3e). The light blue band denotes the acceptable device internal operating window, while the dark blue span represents the expansion of the ambient tolerance range over which the device remains within this window. We define this operating temperature expansion as $\Delta T_1 - \Delta T_2$, the increase in the ambient tolerance range enabled by emissivity modulation.

Initially, the ASPIRE device equilibrates at T_{dev}^{max} and stays in the high-ε state to maximize heat dissipation. As the ambient drops to the switching temperature (T_{swt}), the device switches to the low-ε state to conserve heat. Once the ambient falls below the tunable range, the device follows the environment downward, and switches back to high-ε state upon re-heating. With this mechanism, the ASPIRE device extends the operating temperature expansion range by 4.2 °C, as shown by comparing (ΔT_1 *vs.* ΔT_2), demonstrating its ability to dynamically modulate the heat loss and stabilize temperature against ambient fluctuations. Details of the equilibrium definition and calculation are provided in Note S5.

To further examine the thermoregulation potential of the ASPIRE device, we calculate the accessible operating temperature range expansion under different heat transfer coefficients (h). Fig. 3f shows that the operating temperature expansion range significantly increases with decreasing h, indicating that emissivity tuning has a more substantial effect when radiative heat transfer dominates. Detailed results are presented in Note S6, Fig. S14 and S15. Notably, under minimal h, the ASPIRE device can expand the operating temperature range by as much as 25.6 °C, indicating substantial promise for applications such as spacecraft thermoregulation.

This result, illustrated in Fig. 3f, underscores the potential of the ASPIRE device for aerospace applications. In space, radiation is the sole method of heat transfer to the environment, and spacecraft experience significant thermal cycles when transitioning between solar illumination and shadowed regions. For example, the International Space Station (ISS) orbits the Earth 16 times a day, facing surface temperature ranging from −120 °C to 120 °C.[47] By exploring its rapid and tunable emittance properties, the ASPIRE device can attenuate extreme temperature variations, ensuring stabilized spacecraft temperature and crew safety. Moreover, this solution-processable electrochromic polymer approach offers a lightweight alternative to the conventional mechanical louvers in micro- (<20 kg) and nano- (<2 kg) satellites, thereby advancing next-generation thermal management solutions.[48]

The all-solution-processable fabrication for 3D curved objects

The all-solution-processable fabrication methodology can be applied to a wide variety of 3D curved objects, transforming them into electrochromic, variable-emittance devices. To demonstrate this versatility, we fabricated the ASPIRE device on a copper semisphere ($d \approx 8$ cm), representing a geometry with non-zero Gaussian curvature ($K \neq 0$) that is challenging for traditional planar devices. The fabrication process was optimized to accommodate the complex topography. Specifically, Kapton tape was applied as an insulation layer on the surface of the copper semisphere to leverage its thermal conductivity while preventing direct electrical contact. Subsequently, a layer of filter paper was employed to serve as a porous scaffold for the PAM/LiCl aqueous precursor solution. We employed the viscosity-controlled thermal curing protocol (see Methods for details) to ensure that the electrolyte impregnated the scaffold and formed a uniform coating on the curved surface without running off.

Fig. 4a and b show photographs of the experimental setups and IR thermal images of the semi-spherical ASPIRE device. During testing, the device was heated by a polyimide heater attached to the inner surface to maintain a constant background temperature of 38 ± 0.2 °C. A constant potential of −2 V and 2 V was alternatively applied to the device. The apparent surface temperature of the ASPIRE region changed by 2.3 °C due to emissivity modulation, confirming the device's functionality on doubly curved surfaces. The continuous switching process and dynamic thermal regulation performance can be viewed in Movie S3. While the apparent temperature modulation (2.3 °C) is lower than that of the planar counterpart (6.1 °C), this difference can be largely explained by the thermodynamic and geometric constraints of the setup. First, the lower base temperature (38 °C *vs.* 50 °C) reduces the radiative power contrast by approximately 50% according to the Stefan–Boltzmann law. Second, unlike the planar device fabricated on smooth glass, the curved device utilizes a porous filter paper scaffold. The microscopic roughness of the fibrous interface introduces optical scattering that slightly reduces the specular emissivity contrast. Combined with the geometric view factor of the curved surface, these physical factors align with the observed experimental values. The results for the bulbous copper cup, which represents an arbitrary complex geometry, are provided in Fig. S16 to further demonstrate the versatility of our fabrication strategy. All thermal

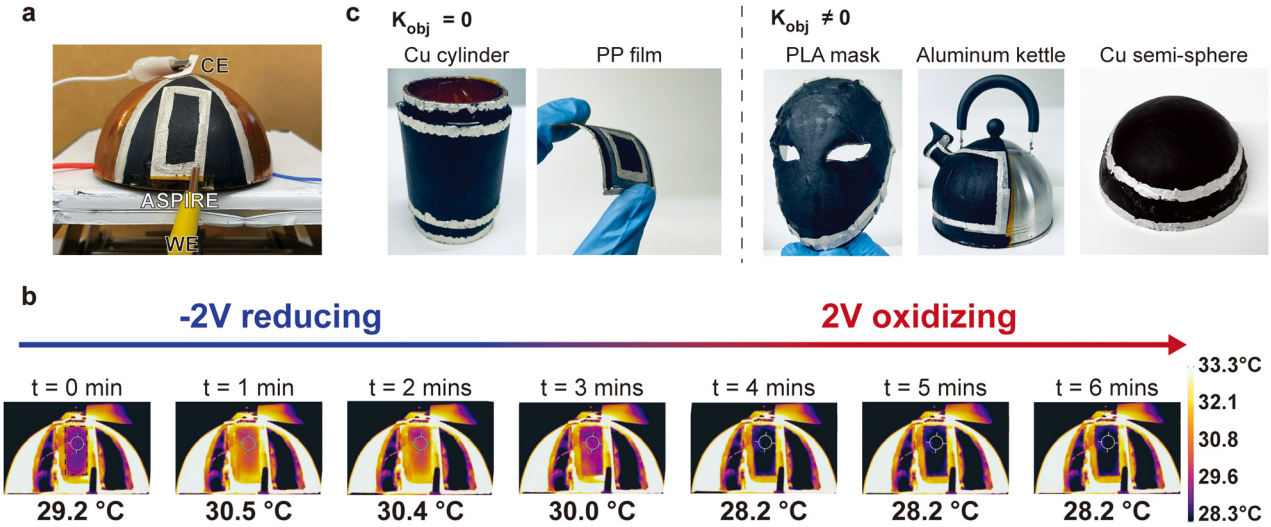

Fig. 4 3D curved ASPIRE devices and their performances. (a) Photo of the semi-spherical ASPIRE device ($d \approx 8$ cm) and the experimental setup. The device was heated by a polyimide heater attached to the inner surface, with the background temperature monitored by a thermocouple. WE: working electrode. CE: counter electrode. (b) Thermal images of the semi-spherical ASPIRE device during electrochemical switching. The maximum apparent temperature difference (ΔT_{max}) is approximately 2.3 °C (30.5 °C at reduced state *vs.* 28.2 °C at oxidized state), achieved by varying the emissivity. The actual temperature of the semi-sphere is held at 38 ± 0.2 °C. The full video of the dynamic switching process is available in Movie S3. (c) Photos of ASPIRE devices fabricated in various shapes on different substrates, demonstrating the remarkable versatility of the all-solution-processed fabrication method.

images were acquired using the same camera configuration with a fixed emissivity setting. Apparent temperature changes were extracted from the same region of interest (ROI) for each state.

Furthermore, Fig. 4c showcases the adaptability of this all-solution-processed fabrication approach, showing its application to various objects, including planar films, cylinders, semi-spheres, curved 3D-printed masks, and water kettles. Most importantly, this methodology is substrate-independent, enabling any insulating substrate to transform into an electrically tunable, variable-emissivity device for thermal regulation and electrochromic applications in numerous fields.

Conclusions and outlook

This research demonstrates that our all-solution-processable fabrication process can be effectively applied to various 3D curved objects, transforming them into dynamically controlled electrochromic devices. By spray-coating carbon nanotubes to form networks, aqueous PEDOT:PSS solution can penetrate these networks and create a heterogeneous mixed ionic–electronic conductor on the object's surface conformally. This layer facilitates simultaneous vertical ion transport and horizontal electrical transport, leading to enhanced electrochromic reactions that can tune the object's emissivity. The FTIR data and thermal images validate the success of this concept, showing a $\Delta\varepsilon = 0.195$ thermal emissivity contrast with robust durability and an apparent temperature difference of 6.1 °C on planar devices and 2.3 °C on 3D curved devices.

Our process addresses the critical challenge of air-gap resistance, which has long been a barrier to effective mid-IR electrochromic thermoregulation on arbitrarily shaped surfaces. To fully realize practical applications, the achieved emissivity modulation ($\Delta\varepsilon = 0.195$) provides a solid baseline. Heat transport simulations confirm that this modulation depth is sufficient to passively expand the operating temperature tolerance by 4.2 °C in mild indoor convection (h = 3 W m^2 K^{-1}). For personal thermal management and enclosed devices, this thermal buffer effectively conserves heat and significantly reduces the energy dependency on active heating systems during environmental fluctuations. Moreover, in extreme, radiation-dominated environments such as space (h = 0 W m^2 K^{-1}), the same modulation depth can expand the operating range by up to 25.6 °C.

Building upon this, future directions will focus on specific strategies to further enhance the emissivity contrast and operational durability. At the material level, developing new conjugated polymers with intrinsically higher charge carrier mobility that remain compatible with non-toxic aqueous processing will be key to breaking the current optical modulation limits. At the structural level, formulating highly viscous gel electrolytes will allow for direct conformal coating without the need for porous fibrous scaffolds. This will minimize microscopic interfacial scattering, thereby maximizing specular infrared reflection and the apparent temperature modulation amplitude on complex 3D geometries. Finally, to guarantee long-term cycle life and enable robust operation without solvent evaporation, transitioning to ionic liquid-based gel electrolytes (ionogels) will be essential. These targeted advancements will help realize a broader range of scalable, lightweight, and efficient thermal management solutions across diverse fields.

Methods

Materials

PEDOT:PSS (Clevios PH1000) was purchased from Heraeus. Lithium chloride (99%, anhydrous), acrylamide (purum, >98%),

N,*N*′-methylenebisacrylamide (99%), ammonium persulfate, *N*,*N*,*N*′,*N*′-tetramethylethylenediamine (99%), acetonitrile (>99.9%, HPLC grade), lithium perchlorate (99+%), were purchased from Sigma-Aldrich. Carbon nanotubes (P3-SWNT) were purchased from Carbon Solutions, Inc. PELCO® Conductive Silver Paint was purchased from Ted Pella (#16062). All chemicals were used as received without further treatment.

Preparation of carbon nanotube (CNT) solution

The carbon nanotube solution recipe was modified from the previous work by Ma *et al.*[49] 20 mg of CNT were dispersed in a mixture of 18 ml of isopropyl alcohol and 2 ml of deionized (DI) water, resulting in a 1 mg ml^{-1} concentration. The solution was sonicated for 2 hours to fully disperse the carbon nanotubes before spray coating processes.

Synthesis of polyacrylamide(PAM)/LiCl hydrogel electrolyte

The PAM/LiCl hydrogel electrolyte was synthesized based on the previous literature.[40,41] 8 M of LiCl salt was dissolved in DI water, and 2.2 M of acrylamide monomer was added into the LiCl solution under stirring. After the acrylamide monomer was fully dissolved, 0.06 wt% of *N*,*N*′-methylenebisacrylamide (MBAm, as the crosslinker) to the weight of acrylamide monomer and 0.17 wt% of ammonium persulfate (APS, as the photoinitiator) to the weight of acrylamide monomer were added into the solution. After MBAm and APS were dissolved, 0.25 wt% of *N*,*N*,*N*′,*N*′-tetramethylethylenediamine (TEMED, as a crosslinking accelerator) to the weight of acrylamide monomer was dropped into the solution under stirring for 2 minutes. The precursor solution was quickly transferred into the object, or a mold and ultraviolet (UV) light was applied (SCOUT UVLED S4020-40K). The crosslinking process finished within 20 minutes, and the PAM/LiCl hydrogel electrolyte was obtained.

Fabrication of ASPIRE device

The bottom layer (as the counter electrode). A hollow copper cup or a 75 mm × 51 mm large glass slide was used as the base substrate. The substrate was pre-cleaned sequentially with detergent, ethanol, and acetone. Prior to spray-coating, the CNT-dispersed solution was sonicated for 2 hours. To insulate the copper cup and eliminate electrical conductivity, Kapton® tape was applied as an insulation layer on the entire copper cup. A spray gun with a 0.8 mm nozzle size was used to coat the CNT solution evenly on the substrate, rotating the substrate 90 degrees every two minutes during the process. Subsequently, PEDOT:PSS PH1000 was poured into a Petri dish, and the CNT-coated substrate was immersed to the PEDOT:PSS solution to form a uniform PEDOT:PSS layer. The coated substrate was left in a fume hood to dry thoroughly.

The middle layer of PAM/LiCl hydrogel solid electrolyte. The middle layer of the PAM/LiCl hydrogel electrolyte was fabricated using either one of three methods: (i) the filter paper method, (ii) the shell mold method, and (iii) the viscosity-controlled thermal curing method.

(i) The filter paper method

The PAM/LiCl precursor solution was prepared as described previously, stopping prior to the addition of TEMED. Filter papers (Whatman, Grade 4) were cut into 9 cm × 5 cm strips and carefully placed on the base substrate with a clean Petri dish positioned underneath to collect any uncross-linked precursor. Following the addition of TEMED, the solution was stirred for three minutes before being evenly distributed over the filter paper. The substrate with filter paper was then subjected to UV light exposure while being rinsed with the precursor solution for 10 minutes. UV curing was continued overnight to ensure complete crosslinking.

(ii) The shell mold method

The PAM/LiCl precursor solution was prepared as previously described. A shell mold with a geometry matching the base substrate but approximately 10% larger was employed. The precursor solution was poured into the shell mold, and the base substrate was placed inside, allowing the solution to fill the gap between the mold and the substrate. UV light was applied to the gap to initiate and complete the crosslinking process. Once crosslinking was achieved, the shell mold was carefully removed, leaving the crosslinked PAM/LiCl hydrogel layer adhered to the base substrate due to its strong adhesive properties.

(iii) The viscosity-controlled thermal curing method (for complex curvatures)

For semi-spherical or other complex curvature substrate, an optimized viscosity-controlled coating protocol was adopted to ensure uniform electrolyte distribution and intimate thermal contact. The PAM/LiCl precursor solution was prepared with the same composition as described above, but without the addition of TEMED. To initiate partial polymerization and increase viscosity, the solution was heated in a 45 °C oil bath for approximately 10 minutes. Once the solution reached a honey-like viscosity, it was immediately quenched in an ice bath to reduce the reaction rate. The viscous precursor was then applied onto a thin, porous filter paper scaffold that was conformally attached to the curved substrate. The viscosity of the precursor solution allowed it to impregnate the scaffold and fill any microscopic gaps between the scaffold and the curved surface, ensuring a continuous thermal interface. Finally, to complete the crosslinking while preventing dehydration, the device was placed in a humidified chamber at 60 °C for 2 hours. The subsequent top-layer CNT spray-coating and PEDOT:PSS dip-coating processes followed the standard procedures described in the next section.

The top layer (as the working electrode). The CNT solution was spray-coated onto the surface of the middle layer of the PAM/LiCl hydrogel electrolyte to serve as the top-layer current collector. To prevent short-circuiting, a piece of transparent PE film with a central hole was placed over the substrate to shield the bottom CNT layer during spray-coating. The PEDOT:PSS PH1000 dip-coating process was repeated to form a uniform electrochromic layer of PEDOT:PSS on the CNT-coated surface. The PEDOT:PSS-coated device was left to dry thoroughly overnight in a fume hood. Once dried, the PE film was removed, and PELCO® Conductive Silver Paint was applied along the circumference of both the top and bottom CNT layers. This

coating enhanced electrical conductivity and protected the CNT layer from mechanical damage.

Electrochemistry

The electrochromic and electrochemical reactions were conducted *via* a Biologic VMP-3 Multichannel Potentiostat or a Biologic SP-150 Potentiostat. For the CNT mass loading optimization (Fig. 2). The cyclic voltammetry was performed at a scan rate of 100 mV s^{-1}. The higher rate was selected to assess the rate capability and minimize the contribution of parasitic leakage currents in the thick composite films. Accordingly, the discharge capacity (Q_{dis}) was calculated by integrating the cathodic current ($I < 0$) to rigorously quantify the accessible charge storage.

For the stability comparison (Fig. S3) between CNT and AgNW-based electrodes, the measurements were conducted at a scan rate of 20 mV s^{-1}. This standard scan rate was chosen to clearly resolve the redox features and monitor the rapid degradation behavior of the AgNW electrodes upon cycling. A commercial non-aqueous Ag^+/Ag reference electrode (CH Instrument) and a platinum wire counter electrode (CH Instrument) were used in the experiments. 0.1 M $LiClO_4$ was dissolved in acetonitrile as the electrolyte.

The ionic conductivity of PAM/LiCl hydrogel electrolyte was measured in a stainless-steel coin cell set and assembled in a glove box filled with argon to prevent side reactions with oxygen. The stainless steel was used as the ion-blocking electrode. The ionic conductivity was calculated based on the following equation:

$$\sigma_{\text{ionic}} = \frac{t}{R_s \times A}$$

where t is the thickness of the PAM hydrogel electrolyte, R_s is the resistivity of the PAM hydrogel electrolyte, and A is the contact area of the coin cell spacer and the PAM hydrogel electrolyte. The resistivity is obtained from the x-axis intersection in the potential electrochemical impedance spectroscopy (PEIS) with a perturbation of 10 mV and a frequency range of 1 Hz to 1 MHz. All measurements were repeated 3 times.

Characterization

Electrical conductivity measurement. The samples' DC electrical resistance was measured using the four-point method, a Signatone Pro4 probe stand with an SP4 probe head, and a Keysight B2901A precision source/measure unit. The thickness of carbon nanotubes was measured using a KLA Tencor P-7 profilometer. All measurements were repeated three times at different places (1 cm away from the sample edges) to obtain an average value.

Structure and morphologies characterization. The STEM and TEM images of the carbon nanotubes were carried out using an aberration-corrected JEOL JEM-ARM200F Scanning Transmission Electron Microscope equipped with a cold emission source operated at 200 kV. The morphologies of the carbon nanotubes were carried out using a Carl Zeiss Merlin high-resolution Field Emission Scanning Electron Microscope (FE-SEM). EDX imaging was acquired by an Oxford Ultim Max 100 EDS detector. A 5 nm Pt/Pd layer was deposited to increase SEM resolution.

Optical measurement. The mid-IR diffused reflectance spectra, ranging from 2.5 μm to 20 μm, were measured by a Thermo Fisher Nicolet™ iS50 FTIR spectrometer with a diffused gold integrating sphere (PIKE Technologies). An e-beam deposited 200 nm gold on a silicon wafer (University Wafer, #1319) was used as the background standard reference. Raman spectroscopy was measured by Horiba LabRAM HR Evolution Confocal Raman Microscope. A 532 nm laser was used to excite the samples on a silicon (111) wafer substrate. The infrared thermal images were captured with an FLIR E53 thermal camera. All the measurements were performed at room temperature.

Infrared (IR) spectroscopic ellipsometry data were collected by IR-VASE Mark II from JA Woollam Co. at angles of incidence equal to 45°, 55°, 65°, and 75° from 2 to 20 μm, on a PEDOT:PSS PH1000 film spin-coated on a Au/Si wafer. The spectroscopic ellipsometry data were fitted with WVASE software to obtain the absorption coefficients.

Porosity measurement

The pore size distribution of CNT was measured by a gas adsorption analyzer (Micromeritics 3Flex). 0.011 g of CNT powder was used as received without further treatment for the experiment. The nitrogen adsorption and desorption isotherms were measured at 77 K. The sample was degassed at 80 °C for 12 hours before the measurement. The CNT pore size distribution was calculated from nitrogen adsorption data using the NLDFT model.

Inductively coupled plasma mass spectrometry (ICP-MS)

A 3% nitric acid solution was used as the diluting matrix for all the Li content measurements. 0.198 g of PAM/LiCl hydrogel was immersed in aqua regia solution for three days to ensure complete dissolution. The resulting supernatant was diluted with a 3% nitric acid solution for later ICP-MS measurement. All measurements were performed using either a Thermo iCAP Q ICP-MS or a Thermo iCAP RQ ICP-MS. The water content in the PAM/LiCl hydrogel sample was determined before and after the lyophilization process. The process involved 24 hours of freezing at −80 °C in a Thermo-Fisher TSX Series Ultra-Low Freezers and 72 hours of vacuum drying in a FreeZone 6 Liter −50C Console Freeze Dryer.

Author contributions

P.-C.H. and P.-J.H. conceived the idea. P.-J.H. designed and carried out the device fabrication process of ASPIRE, mid-IR optical property characterization, Raman, and electrochemical measurement. Q.L. simulated the radiative power and comfort zone expansion under various circumstances. T.-H.C. and C.-T.F. optimized the PAM synthesis and coating process. X. W. synthesized polyaniline and performed spectroscopic ellipsometry and 4-point probe measurement. R.W. carried out adsorption isotherm measurements and pore distribution analysis. Q.F. and Y.H. assisted in data analysis and data visualization. Y.H. assisted with SEM and EDX characterization. G.Y. carried out ICP-MS experiments. F.S. assisted with STEM and TEM characterization.

Y.Z. and C.S. assisted with the electrochemical experiments and EIS measurements. G.H. assisted with the spray coating processes. P.-R.H. conducted lyophilization processes. J.L., Y.C. and A.F. assisted with the preparation of samples. P.-J.H. and P.-C.H. wrote the manuscript with input from all coauthors.

Conflicts of interest

The authors declare no conflict of interest.

Data availability

All data are present in the manuscript and the supplementary information (SI). The supplementary information includes supplementary figures and tables, additional experimental details, thermal simulations, electrochemical characterization, cycling and switching analyses, and supplementary movies related to device operation on planar and curved substrates. See DOI: https://doi.org/10.1039/d5mh02110c.

Additional data related to this paper are available from the corresponding authors upon reasonable request.

Acknowledgements

The project is sponsored by the startup fund of the Pritzker School of Molecular Engineering, University of Chicago. P.-C. H. and P.-J. Hung gratefully acknowledge support from the National Science Foundation under award number NSF ECCS-2324286. This work made use of the shared facilities at the University of Chicago Materials Research Science and Engineering Center, supported by the National Science Foundation under award number DMR-2011854. Parts of this work were carried out at the Soft Matter Characterization Facility of the University of Chicago. This work made use of the Pritzker Nanofabrication Facility part of the Pritzker School of Molecular Engineering at the University of Chicago, which receives support from Soft and Hybrid Nanotechnology Experimental (SHyNE) Resource (NSF ECCS-1542205), a node of the National Science Foundation's National Nanotechnology Coordinated Infrastructure. This work made use of instruments in the Electron Microscopy Core of UIC's Research Resources Center. Acquisition and upgrade of the UIC JEOL JEM ARM200CF was supported by an MRI-R grant (DMR-0959470) and an MRI grant (DMR-1626065) from NSF. We would like to thank Dr Chi-Chang Hu (National Tsing Hua University, Taiwan) for the discussion. We acknowledge Dr Joseph G. Manion (CGFigures) for sharing carbon nanotube 3D models under a CC0 1.0 public-domain dedication. This work makes use of public domain resources available in the CGFigures Asset Library created by Dr J. G. Manion.

References

1 J. Niu, *et al.*, Infrared electrochromic materials, devices and applications, *Appl. Mater. Today*, 2021, **24**, 101073.
2 X. Guo, *et al.*, Dynamic photothermal modulation in energy-efficient buildings, *Mater. Today*, 2025, **91**, 84–102.
3 J. Wang, *et al.*, Roadmap for electrochromic smart devices: From materials engineering and architectures design to multi-functional application, *Prog. Mater. Sci.*, 2025, **153**, 101461.
4 T. H. Chen and P. C. Hsu, Wearable variable-emittance devices-The future of dynamic personal thermoregulation, *Appl. Phys. Lett.*, 2024, **125**, 180501.
5 P. C. Hsu, *et al.*, A dual-mode textile for human body radiative heating and cooling, *Sci. Adv.*, 2017, **3**, e1700895.
6 P. C. Hsu, *et al.*, Radiative human body cooling by nanoporous polyethylene textile, *Science*, 2016, **353**, 1019–1023.
7 T.-H. Chen, *et al.*, A kirigami-enabled electrochromic wearable variable-emittance device for energy-efficient adaptive personal thermoregulation, *PNAS Nexus*, 2023, **2**, pgad165.
8 A. P. Raman, M. A. Anoma, L. Zhu, E. Rephaeli and S. Fan, Passive radiative cooling below ambient air temperature under direct sunlight, *Nature*, 2014, **515**, 540–544.
9 S. Fan and W. Li, Photonics and thermodynamics concepts in radiative cooling, *Nat. Photonics*, 2022, **16**, 182–190.
10 X. A. Zhang, *et al.*, Dynamic gating of infrared radiation in a textile, *Science*, 2019, **363**, 619–623.
11 Y. Peng and Y. Cui, Advanced textiles for personal thermal management and energy, *Joule*, 2020, **4**, 724–742.
12 R. H. Wu, T. H. Chen and P. C. Hsu, Stay healthy under global warming: a review of wearable technology for thermoregulation, *Ecomat*, 2023, **5**, e12396.
13 C. Sui, *et al.*, Dynamic electrochromism for all-season radiative thermoregulation, *Nat. Sustainability*, 2023, **6**, 428–437.
14 S. M. Zhao, *et al.*, An electro-driven dynamic and multicolored radiative thermal regulation material for all-year-round building energy saving, *Adv. Funct. Mater.*, 2024, 2419378.
15 Z. W. Shao, *et al.*, Tri-band electrochromic smart window for energy savings in buildings, *Nat. Sustainability*, 2024, **7**, 796–803.
16 Y. Rao, *et al.*, Ultra-wideband transparent conductive electrode for electrochromic synergistic solar and radiative heat management, *ACS Energy Lett.*, 2021, **6**, 3906–3915.
17 H. Demiryont and D. Moorehead, Electrochromic emissivity modulator for spacecraft thermal management, *Sol. Energy Mater. Sol. Cells*, 2009, **93**, 2075–2078.
18 P. Chandrasekhar, *et al.*, Variable-emittance infrared electrochromic skins combining unique conducting polymers, ionic liquid electrolytes, microporous polymer membranes, and semiconductor/polymer coatings, for spacecraft thermal control, *J. Appl. Polym. Sci.*, 2014, **131**, 40850.
19 Q. Fan, *et al.*, Dynamic thermoregulatory textiles woven from scalable-manufactured radiative electrochromic fibers, *Adv. Funct. Mater.*, 2024, **34**, 2310858.
20 D. E. Shen, C. L. Goins, A. L. Jones, A. M. Österholm and J. R. Reynolds, Design rules for high contrast mid-infrared electrochromism in conjugated polymers, *ACS Mater. Lett.*, 2024, **6**, 528–534.
21 A. L. Dyer, E. J. Thompson and J. R. Reynolds, Completing the color palette with spray-processable polymer electrochromics, *ACS Appl. Mater. Interfaces*, 2011, **3**, 1787–1795.

22 J. Jensen, M. Hösel, A. L. Dyer and F. C. Krebs, Development and manufacture of polymer-based electrochromic devices, *Adv. Funct. Mater.*, 2015, **25**, 2073–2090.
23 J. Padilla, A. M. Österholm, A. L. Dyer and J. R. Reynolds, Process controlled performance for soluble electrochromic polymers, *Solar Energy Materials and Solar Cells*, 2015, **140**, 54–60.
24 L. Nayak, S. Mohanty, S. K. Nayak and A. Ramadoss, A review on inkjet printing of nanoparticle inks for flexible electronics, *J. Mater. Chem. C*, 2019, **7**, 8771–8795.
25 J. R. Reynolds, B. C. Thompson and T. A. Skotheim, *Conjugated Polymers: Properties, Processing, and Applications*, 4th edn, CRC Press, 2019.
26 Q. Li, T.-H. Chen and P.-C. Hsu, Use electrochemistry to charge the next dynamic thermal metamaterials, *Next Energy*, 2024, **3**, 100108.
27 Y. Zhou, *et al.*, Electrochromic smart windows with on-demand photothermal regulation for energy-saving buildings, *Adv. Mater.*, 2025, **37**, e2502706.
28 C. Hu, *et al.*, Crystal reconstructed cubic nickel oxide with energetic reactive interfaces for exceptional electrochromic smart windows, *Mater. Horiz.*, 2025, **12**, 1962–1970.
29 Z. Mei, *et al.*, A colorful electrochromic infrared emissivity regulator for all-season intelligent thermal management in buildings, *Adv. Mater.*, 2025, **37**, e2420578.
30 K. F. Gauss, *General Investigations OF Curved Surfaces*, The Princeton University Library, 1827.
31 M. Heydari Gharahcheshmeh and K. K. Gleason, Texture and nanostructural engineering of conjugated conducting and semiconducting polymers, *Mater. Today Adv.*, 2020, **8**, 100086.
32 D. Fu, *et al.*, Differentiation of gas molecules using flexible and all-carbon nanotube devices, *J. Phys. Chem. C*, 2008, **112**, 650–653.
33 P. Tan, F. Lu and Y. Han, Mid-infrared optimized electro-reflective device based on PEDOT/PSS, *Sol. Energy Mater. Sol. Cells*, 2021, **219**, 110808.
34 A. Thess, *et al.*, Crystalline ropes of metallic carbon nanotubes, *Science*, 1996, **273**, 483–487.
35 J. P. Lu, Elastic properties of carbon nanotubes and nanoropes, *Phys. Rev. Lett.*, 1997, **79**, 1297–1300.
36 J.-P. Salvetat, *et al.*, Elastic and shear moduli of single-walled carbon nanotube ropes, *Phys. Rev. Lett.*, 1999, **82**, 944–947.
37 Á. Szabados, L. P. Biró and P. R. Surján, Intertube interactions in carbon nanotube bundles, *Phys. Rev. B: Condens. Matter Mater. Phys.*, 2006, **73**, 195404.
38 T. Kress, X. Liu and A. C. Forse, Pore network tortuosity controls fast charging in supercapacitors, *Nat. Mater.*, 2026, **25**, 440–446.
39 J. W. Haverkort, A theoretical analysis of the optimal electrode thickness and porosity, *Electrochim. Acta*, 2019, **295**, 846–860.
40 H. Li, *et al.*, Ultraflexible and tailorable all-solid-state supercapacitors using polyacrylamide-based hydrogel electrolyte with high ionic conductivity, *Nanoscale*, 2017, **9**, 18474–18481.
41 T. G. Yun, *et al.*, All-transparent stretchable electrochromic supercapacitor wearable patch device, *ACS Nano*, 2019, **13**, 3141–3150.
42 V. Bocharova and A. P. Sokolov, Perspectives for polymer electrolytes: a view from fundamentals of ionic conductivity, *Macromolecules*, 2020, **53**, 4141–4157.
43 P. R. Somani and S. Radhakrishnan, Electrochromic materials and devices: present and future, *Mater. Chem. Phys.*, 2003, **77**, 117–133.
44 R. Wu, B. D. Paulsen, Q. Ma and J. Rivnay, Mass and charge transport kinetics in an organic mixed ionic–electronic conductor, *Chem. Mater.*, 2022, **34**, 9699–9710.
45 S. T. Keene, A. Rao and G. G. Malliaras, The relationship between ionic–electronic coupling and transport in organic mixed conductors, *Sci. Adv.*, 2023, **9**, eadi3536.
46 G. Rebetez, O. Bardagot, J. Affolter, J. Réhault and N. Banerji, What drives the kinetics and doping level in the electrochemical reactions of PEDOT:PSS?, *Adv. Funct. Mater.*, 2022, **32**, 2105821.
47 E. A. Ryan, Z. D. Seibers, J. R. Reynolds and M. L. Shofner, Electrically conducting polymers and composites for applications in space exploration, *J. Appl. Polym. Sci.*, 2024, **141**(15), e55225.
48 J. Liang, *et al.*, Ionic Liquid-Based Reversible Metal Electrodeposition for Adaptive Radiative Thermoregulation Under Extreme Environments, *Adv. Funct. Mater.*, 2025, **36**, 2419087.
49 R. Ma, *et al.*, Highly efficient electrocaloric cooling with electrostatic actuation, *Science*, 2017, **357**, 1130–1134.